Simulation-Aided Measurement-Based Channel Modeling for Propagation at 28 GHz in a Coniferous Forest

Yaguang Zhang, John A. Tan, Bryan M. Dorbert, Christopher R. Anderson, and James V. Krogmeier

***Abstract*—The high cost required by traditional measurement campaigns often limits the amount of data that can be obtained, to the detriment of data-intensive modeling techniques such as machine learning. This work addresses the limitations from the measurement system and environment by changing the traditional channel modeling approach. Simulation was used as an auxiliary means to obtain data, showing the broader applicability of a site-specific model. More specifically, we explore the possibility of augmenting channel measurements with simulation predictions to acquire comprehensive sets of mm-wave channel information for improved modeling. Path loss measurements from a 28-GHz campaign in a coniferous forest were utilized in conjunction with semi-empirical statistical ray tracing simulations to evaluate the performance of measurement-based channel models beyond the specific measurement region from which they were developed. The root-mean-square deviations between model predictions and simulation results are 11.3 dB for an ITU woodland model and 6.8 dB for a site-specific model we published in a previous manuscript. Furthermore, the site-specific model was demonstrated to agree with simulation predictions at distances and locations we were unable to measure. These results show a broad applicability of our site-specific model as well as a mechanism to derive accurate models from a combination of measurement and simulation data.**

***Index Terms*—Millimeter wave, ray tracing, simulation-aided channel modeling, site-specific models.**

I. Introduction

With the rapid development of next-generation wireless communication systems, millimeter-wave (mm-wave) channel measurement and modeling have attracted extensive attention worldwide from academia and industry [1]. Because traditional channel modeling depends primarily on measurement results, many intensive mm-wave measurement campaigns have been carried out for a variety of environments during the past decade [2]–[6], boosting our knowledge on mm-wave propagation characteristics. However, the high cost required by measurement campaigns, both in money and time, often prevents researchers from obtaining as many measurement results as desired. This problem is exacerbated when data-hungry techniques, such as machine learning, are applied to propagation modeling or spectrum management [7]. As a result, these scenarios have heavily utilized simulation for mm-wave channel information acquisition [8]–[10]. Moreover, the simulated channel characteristics attached to the locations [11], [12] where those techniques are expected to be implemented are often left unverified. The confidence in applying simulation to channel modeling and spectrum management in real-world scenarios would be dramatically increased if these simulation results are tested and verified using measured data.

In this paper, we explore the possibility of augmenting measurement-based propagation models with extensive simulation datasets. Results from a 28-GHz measurement campaign following ten tracks in a coniferous forest were utilized to construct site-specific path loss models in [12]. The measurement locations were then input to a radio frequency (RF) simulation engine developed by CSLabs [13]. Simulation results were compared with measurements point-by-point, which yielded a typical root-mean-square error (RMSE) of approximately 10 dB. Next, the area of interest was expanded to contain locations not covered by the measurements, including those inaccessible during the campaign, to generate a much larger set of propagation information from the simulation engine. This simulation dataset was used to evaluate our *site-specific model C* [12] and the ITU-R obstruction by woodland model (referred to as the ITU model for short in this paper) [14], both of which were designed for propagation through forest environments. The root-mean-square deviations (RMSDs) between model predictions and simulation results are 6.8 dB for our site-specific model and 11.3 dB for the ITU model, which supports the applicability of the site-specific model beyond the measurement region covered in the campaign.

The paper is organized as follows. In Section II, we present the setups for the measurement and the simulation. The corresponding results are compared in Section III. Then, the extended simulation dataset and its example application in channel modeling are described in Section IV. Finally, in Section V, we conclude the paper.

II. Measurement and Simulation Setups

A. Measurement Setup

A custom-designed broadband sliding correlator sounder was utilized to record channel measurements along ten different tracks covering a coniferous forest in Boulder, Colorado. The system used horn antennas with a nominal 15° half-power beamwidth on both the transmitter (TX) and the receiver (RX) sides. The TX was located just outside of a lightly forested region, as shown in Fig. 1(a). Table I summarizes the key specifications for the sounder. More information on the measurement campaign and its results can be found in [12].

Y. Zhang and J. V. Krogmeier are with the School of Electrical and Computer Engineering, Purdue University, 465 Northwestern Avenue, West Lafayette, IN 47907, USA. (Email: {ygzhang, jvk}@purdue.edu)

J. A. Tan and B. M. Dorbert are with SciX3, LLC. (dba CSLabs), 6154 McLendon Court, Alexandria, VA 22310, USA. (Email: {jtan, bdorbert}@cslabs.tech)

C. R. Anderson is with the Department of Electrical and Computer Engineering, United States Naval Academy, 105 Maryland Ave, Annapolis, MD 21402, USA. (Email: canderso@usna.edu)

Sponsorship was provided for this work by NSF grant 1642982 and for the CSLabs simulation engine by DARPA contract W31P4Q-14-C-0014.

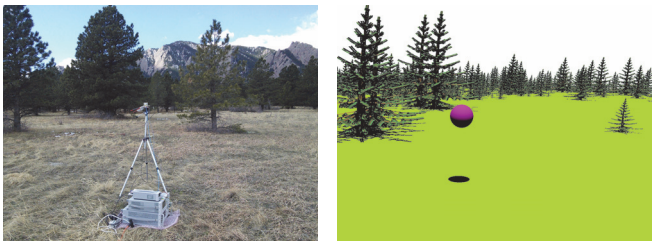

(a) In the measurement campaign (b) In simulation

Fig. 1. The measurement environment from the TX's view for both (a) the measurement campaign and (b) the reconstructed scene in the RF simulator.

B. Simulation Setup

The simulation engine [13], designed for RF propagation in high foliage environments, was utilized to reconstruct the measurement scene and obtain path loss predictions. This engine uses a semi-empirical statistical (SES) approach that has been demonstrated to produce accurate modeling with general scene details once it has been calibrated with a small set of measured data. Fig. 2 illustrates the structure of the engine with a block diagram. Records from the measurement campaign and public geographic datasets were aggregated for the scene generation module to reconstruct the measurement environment. Then, the ray tracing and sampling module performed the multipath calculations and recorded rays incident on a RX location. Finally, an empirical calibration [15] was carried out for the simulation output with the measurement results. These operations will be briefly described below.

1) Environment Reconstruction: To reconstruct the measurement environment in line with the simulation engine, we aggregated data from different sources. The ground profile was obtained by linearly interpolating the 1/3rd arc-second digital elevation models from the United States Geological Survey (USGS) over the area of interest. Manually labeled tree trunk locations from the measurement campaign records were used to add coniferous tree models. LiDAR data was also fetched from USGS and each tree's height was set according to the difference between the LiDAR data z value and the USGS ground elevation for that tree's trunk location. During the measurement campaign, the shortest plants we observed were bushes with a height of roughly one meter, so a minimum allowable tree height of one meter was also enforced. The locations for the TX and the RX were fetched from the GPS records of the measurement campaign. The scene generation module then generated a three-dimensional (3D) environment model accordingly. Fig. 1(b) demonstrates the reconstructed

TABLE I
SLIDING CORRELATOR CHANNEL SOUNDER SPECIFICATIONS

Carrier Frequency	28 GHz
Chip Sequence Length	2047
RF Bandwidth (First Null)	800 MHz
TX Chip Rate	400 Mcps
RX Chip Rate	399.95 Mcps
TX Power	23 dBm
TX/RX Antenna Gain	22 dBi

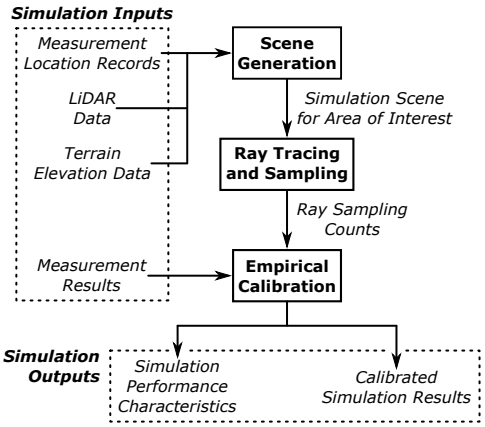

Fig. 2. Block diagram for the simulation engine.

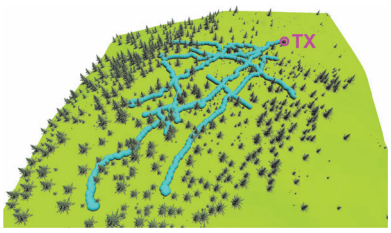

Fig. 3. A bird's-eye view for the reconstructed measurement environment.

environment seen by the TX. A bird's-eye view for the whole scene with all measured RX locations can be found in Fig. 3.

2) SES Approach and Empirical Calibration: The key for the simulation engine to enable high-accuracy ray tracing with low computational complexity is the SES approach. It applies statistical ray sampling with an empirical calibration to generate simulation results that closely match the measurement data. More specifically, the SES model applies path tracing to determine propagation quantities such as path loss and delay spread through statistics of the ray interaction with the environment. This is achieved by the ray tracing and sampling module, which models and propagates the RF signal as rays between TXs, foliage clusters, RXs, and other scene elements such as terrain features. Other features, such as atmospheric refractivity or additional wave phenomenology, can be included as necessary. For simplicity, our simulations considered free-space path loss and ground reflection besides foliage effects. As rays (discrete beams in our setup) are traced through the scene, they maintain state information due to scattering caused by scene elements. When rays exit the computational volume, they are terminated. Rays that arrive at the RX are recorded. The number of rays that propagate through a given environment from TX to RX, which we define as "ray sampling counts", is proportional to the power incident on the RX. The ray sampling counts provide a statistical metric for the corresponding RF pathway and are fed into the empirical calibration module for the final simulation output.

Empirical calibration for RX power is performed to match the simulator output with measured data via a "zero-span" technique for obtaining a linear relationship between ray sampling counts and the total received power. The "zero" point is set by the measurement system noise floor, which could

be determined by averaging recordings taken when the TX is turned off or extracted from a measured dataset by the use of median filters. The "span" is then set by defining a constant of proportionality between the measured received power at a measurement location and the ray sampling counts at that same location. Calibration procedures for our scenario (path loss instead of RX power) are derived accordingly in Section III-A.

III. Simulator Performance Evaluation

In this section, we obtain simulation path loss values for the measured locations using isotropic antenna settings and evaluate the simulation engine's performance accordingly. Calibration was conducted for each individual track; RMSE was evaluated both track-by-track and for track groups.

A. Empirical Calibration for Path Loss

With the specific foliage laydown of the reconstructed measurement environment, quantities such as power, time delay, delay spread, and arrival angles, can be calculated by the simulation engine. In this paper, we are interested in the RX power P_{RX} so that path loss can be computed for mm-wave channel modeling. The RX path loss calculations follow the relationships:

$$\begin{cases} P_{RX}^{(Sim,\ dBW)} \propto 10\log_{10}\left(S^{\alpha}\right) = 10\alpha\log_{10} S \\ S \propto N(f,E) \end{cases}, \quad (1)$$

where $P_{RX}^{(Sim,\ dBW)}$ is the simulation RX power in dBW without noise, S is the simulation signal strength in W, N is the ray sampling counts on RX, f is the signal frequency, E is the simulation environment (including all objects in the scene with their geometries and material properties), and α is a constant determined empirically, similar to forms used in traditional propagation models. For example, ITU-R 833.9 [14] defines the maximum attenuation A_m as $A_m = A_1 f^{\alpha}$, where A_1 and α are determined empirically. It is also worth noting that N is a function (of f and E) evaluated by the ray tracing and sampling module. Intuitively, Equation (1) assumes (i) the RX power in dB is proportional to the simulation signal power with an adjustment term α, and (ii) the simulation signal strength is proportional to the ray sampling counts. By assigning multiplication factors a and b to these proportional relationships, we can simplify the RX power calculation to:

$$\begin{aligned} P_{RX}^{(Sim,\ dBW)} &= a \cdot 10\alpha\log_{10}\left[bN(f,E)\right] \\ &= (a\alpha)\cdot 10\log_{10}\left[N(f,E)\right] + 10a\alpha\log_{10} b \\ &= \hat{a}N^{(dB)} + \hat{b}\ , \end{aligned} \quad (2)$$

where we have constants $\hat{a} = a\alpha$ and $\hat{b} = 10a\alpha\log_{10} b$, along with the ray sampling counts in dB:

$$N^{(dB)} = 10\log_{10}\left[N(f,E)\right]. \quad (3)$$

Next, we apply the noise floor compensation discussed in Section II-B2 in order to get the final simulated RX power in dBW, denoted by $P_{RX}^{(dBW)}$, which provides a value that can be directly compared against measurement results:

$$P_{RX}^{(dBW)} = P_{RX}^{(Sim,\ dBW)} + P_{noise}^{(dBW)}\ , \quad (4)$$

where $P_{noise}^{(dBW)}$ is the effective noise floor of the measurement system in dBW. Finally, the simulated path loss in dB $PL_{RX}^{(dB)}$ can be obtained by comparing $P_{RX}^{(dBW)}$ with the RX power in dBW for a reference location, denoted here by $P_{ref}^{(dBW)}$:

$$PL_{RX}^{(dB)} = P_{ref}^{(dBW)} - P_{RX}^{(dBW)} + PL_{ref}^{(dB)}\ , \quad (5)$$

where $PL_{ref}^{(dB)}$ is the path loss in dB experienced at the reference location, since $P_{RX}^{(dBW)} + PL_{RX}^{(dB)} = P_{ref}^{(dBW)} + PL_{ref}^{(dB)}$ is the TX power. Assuming a homogeneous environment—so that $\hat{a}$, $\hat{b}$ and $P_{noise}^{(dBW)}$ are the same for both the reference location and the RX—we can apply Equations (2) and (4) in Equation (5) for both the reference and RX locations:

$$\begin{aligned} PL_{RX}^{(dB)} &= \left(\hat{a}N_{ref}^{(dB)} + \hat{b} + P_{noise}^{(dBW)}\right) \\ &\quad - \left(\hat{a}N_{RX}^{(dB)} + \hat{b} + P_{noise}^{(dBW)}\right) + PL_{ref}^{(dB)} \\ &= \hat{a}\cdot\left(N_{ref}^{(dB)} - N_{RX}^{(dB)}\right) + PL_{ref}^{(dB)}\ , \end{aligned} \quad (6)$$

where $N_{ref}^{(dB)}$ and $N_{RX}^{(dB)}$ are the ray sampling counts from the simulation engine in dB for the reference location and the RX, respectively. Because the ray sampling counts are self-consistent in each run of simulation, we can arbitrarily choose one RX location as the reference point and get the ray sampling count difference in dB for the remaining RX locations. Then, we can empirically determine the constants $\hat{a}$ and $PL_{ref}^{(dB)}$ with the measurement data by minimizing RMSE.

B. Track-Wise Comparison of the Measurement Locations

During the campaign, we conducted ten separate measurement runs, each following one continuous track in the forest. The first five tracks are parallel to the TX main beam (moving away/toward the TX) and the other five are transverse to the TX main beam (perpendicular to the parallel tracks). A dedicated simulation was carried out for each track. According to Equation (6), there is a linear relationship between the simulated path loss and the ray sampling count difference. Thus, we can test whether the simulation is valid before the empirical calibration by plotting the measured path loss values along with the corresponding ray sampling count difference values (in replacement of the simulated path loss) in dB over the same metric, for instance, RX-to-TX distance in Fig. 4. Then, if the simulation is valid, the trends of the resulting curves should agree with each other. In our work, the RX-to-TX distance is evaluated in 3D space considering terrain elevation and antenna heights. The two tracks shown in Fig. 4 span the longest over the RX-to-TX distance among the parallel and transverse tracks, respectively. To aid the trend comparison, two vertical axes are used here, the left y axis for the simulated ray sampling count difference while the right y axis for the measured path loss values. Visual comparison suggests that the simulation matches the measured data, especially for some peak and valley locations.

To quantify the performance of the simulation engine, we carried out empirical calibration with the first location on each track as the reference point. After $\hat{a}$ and $PL_{ref}^{(dB)}$

(corresponding to a vertical stretching and a vertical shift of the simulation results in Fig. 4) are determined by the calibration, the resultant simulated path loss should match the measurements in value. Corresponding RMSEs are summarized in the track-wise comparison row of Table II. Most of the RMSEs are around 10 dB, with the overall RMSE being 17.8 dB. For comparison, all traditional channel models in [12] have a RMSE over 20 dB relative to the measured data.

It is worth noting that the simulator works better for parallel tracks, with an impressive overall RMSE of 11.2 dB. For transverse tracks, the RMSE is higher at 25.8 dB. This is caused by the limited accuracy of the measurement records. GPS data obtained from USRP B200 typically has a meter-level error, as do the manually labeled trunk locations (which can be observed in Fig. 1). Given that mm-waves are extremely sensitive to blockage [11], an error of one meter, either from the RX location or the tree locations, could change a line-of-sight (LoS) path to a blocked one and vice versa. For parallel tracks, this disagreement over small-scale fading is less of an issue because these tracks span a long RX-to-TX distance range and large-scale effects dominate in the change of path loss. However, for the transverse tracks, small-scale fading plays a key role in the path loss changes, requiring higher-accuracy location information for a good match. This also contributes to the more noticeable trend difference in Fig. 4(b) compared with Fig. 4(a).

IV. Channel Modeling with Measurement-Based Simulation Data

Using the calibrated simulator, we expanded the area of interest to acquire a comprehensive dataset of simulated path loss values for performance evaluation of the ITU and our site-specific channel models beyond the measured locations.

A. Extended RX Location Grid

An extended RX location grid was generated to cover the new area of interest, as illustrated in Fig. 5. There were sharp drop-offs to the northwest and southeast sides of the measurement site, so the extended area was constrained to the region that was reasonably flat. It has a maximum range of over 510 m, significantly larger than that for our measurement data (around 305 m). The grid contains 5742 points covering 89 229 m^2 with a spatial resolution of 3.9 m between adjacent points. After we obtained the ray sampling counts for the grid from the simulation engine, the path loss empirical calibration was carried out with all the measurement results used as the ground truth path loss values at their nearest-neighbor grid points. The corresponding RMSE values are summarized in the extended grid row of Table II. As we can see, calibration over the whole measurement dataset behaves worse than that carried out separately for each track, because the environment for each track varies slightly (for example, in RX gain, antenna pointing direction, vegetation type, and foliage density). Still, the RMSE for half of the tracks are below 15 dB and the overall RMSE of 23.9 dB is competitive with traditional channel models. For the parallel tracks, the RMSE is significantly lower at 16.3 dB, again because large-scale effects dominate the path loss change.

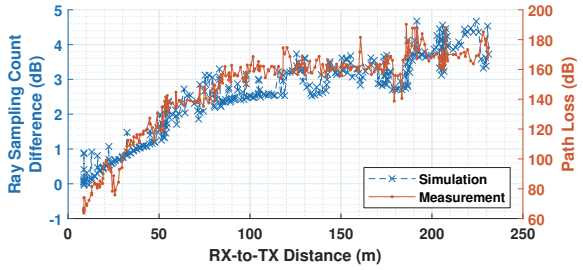

(a) Track 1 (parallel)

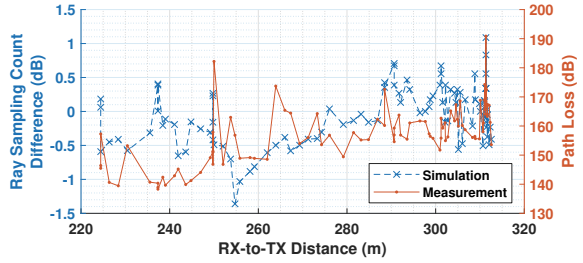

(b) Track 8 (transverse)

Fig. 4. Comparison between the simulation and measurement results before the empirical calibration. (a) Track 1 is the longest track among the ten tracks followed in the measurement campaign. (b) Track 8 is the transverse track which spans the most along the RX-to-TX distance axis.

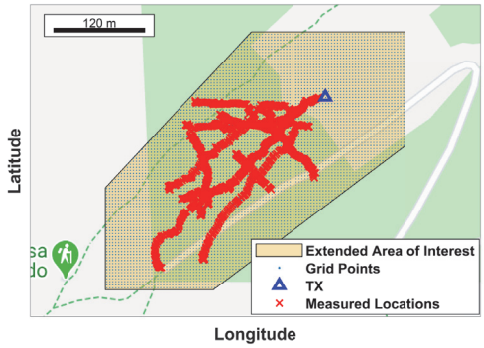

Fig. 5. Overview for the extended area of interest and the corresponding simulation RX grid. The TX and the measured tracks are shown as reference.

B. Channel Model Comparisons

The simulation path loss values for the grid are illustrated in Fig. 6(a). We also obtained corresponding predictions from the ITU model and our site-specific model, as shown in Fig. 6(b) and Fig. 6(c), respectively. We can now use the simulation results as ground truth and test the performance of these two models. By comparing these figures, we can easily identify the most significant limitation of the ITU model: it does not incorporate the site-specific features of the scenario. The ITU model only uses the total path length within the woodland, which increases gradually as the RX moves deeper into the forest, regardless of tree locations and the foliage density. At lower frequencies, this is less of an issue, as trees in a lightly forested area may still be less than a wavelength apart. For mm-wave frequencies, however, even small gaps between trees comprise hundreds of wavelengths, where the influence of site-specific features becomes prominent. Our site-specific model, on the other hand, is based on the total foliage area within the first Fresnel zone, which is computed for each TX-to-RX link

TABLE II
OVERALL PERFORMANCE OF THE SIMULATION RESULTS RELATIVE TO MEASUREMENT DATA

RMSE (dB)	Track #										Parallel (Tracks 1–5)	Transverse (Tracks 6–10)	All
	1	2	3	4	5	6	7	8	9	10			
Track-Wise Comparison	12.4	10.9	9.2	10.2	11.9	35.3	22.7	9.8	10.9	24.2	11.2	25.8	17.8
Extended Grid	20.7	13.3	13.9	11.3	14.2	39.1	42.8	11.3	15.2	26.1	16.3	33.5	23.9

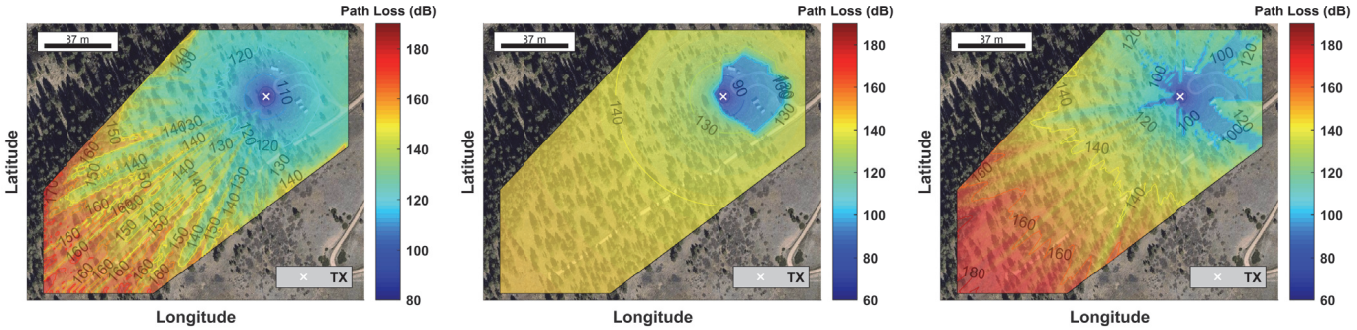

(a) Simulation results (b) ITU model predictions (c) Site-specific *model C* predictions

Fig. 6. Path loss results for the extend RX location grid from the scenario-tuned ray tracing simulation engine, the ITU-R obstruction by woodland model, and our vegetation-area-based site-specific model, respectively.

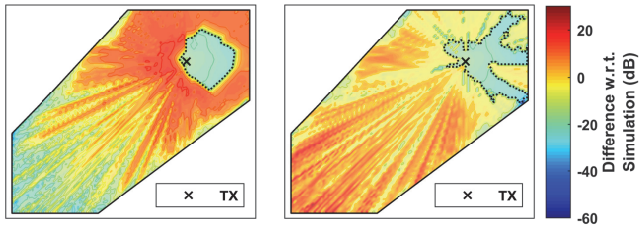

(a) ITU (b) Site-specific *model C*

Fig. 7. Difference between model predictions and simulation results over the extended grid. (a) The ITU model outputs higher path loss than the simulation near the forest edge (indicated by the dotted line). (b) Site-specific *model C* outputs higher path loss than the simulation in deep forest. The region with zero foliage area is illustrated by the dotted-line polygon.

according to high-accuracy LiDAR data. Its prediction pattern reflects link-specific blockage conditions and results in a better agreement with the simulation dataset.

The difference between the model predictions and the simulation results are plotted in Fig. 7. Note that neither of the models is designed for the grassland area near the TX. For the ITU model, that region corresponds to the manually plotted polygon for the forest edge. For our site-specific model, it consists of the RX locations with no obstacles according to the LiDAR data. Their results are shown for a visually consistent comparison region. Relative to the simulation results, the ITU model outputs higher path loss near the forest edge and lower path loss in the LoS region as well as far deep in the forest, while the site-specific model outputs higher path loss in the forest and lower path loss in the LoS region. It is also worth noting that our site-specific *model C* is very accurate in detecting blockages (including those caused by buildings ignored in the simulation) because it enforces a sudden jump of path loss when the first Fresnel zone is obstructed by the first object in the link. The result is step changes in path loss near the TX, where only a few trees are present. This behavior was also observed in the limited number of close-in measurements.

Fig. 8 compares the model performance for the grid. To eliminate biased results from propagation over the grassland, we omitted locations which are out of the forest or have no foliage obstruction in the first Fresnel zone (illustrated by the dotted-line polygons in Fig. 7). As can be seen in Fig. 8(a), the site-specific model has a better agreement with the simulation results in forested areas. This is also shown in Fig. 8(b), where the regional RMSD values evaluated with a 10-m-wide sliding window are plotted against the RX-to-TX distance. The site-specific model outperforms the ITU model by over 10 dB at both the near and far ends. The overall RMSD between model predictions and the in-forest simulation results are 11.3 dB for the ITU model and 6.8 dB for the site-specific model. We can further reduce the RMSD to 5.6 dB if we refit the site-specific model to the in-forest simulation results, which ($L_0 \approx 22.26$ dB, $L_1 \approx 0.41$ dB/m^2, $L_2 \approx 0.16$ dB/m^2, and $A_f \approx 35.92$ m^2) improves the model performance at the far end as can be observed in Fig. 8(b). As a comparison, the RMSEs relative to the measurement dataset are 20.1 dB for the ITU model and 19.2 dB for the site-specific model [12].

Traditional channel models, like the ITU model, emphasize the universal applicability. That is, models are expected to work for all locations with the same environment class, regardless of their varying geographic features. However, for mm-wave, site-specific information becomes so prominent that it needs to be better embedded in the models, which is the key for the performance improvement we saw.

C. Discussion

We have used measurement-calibrated simulation results to evaluate the performance of the ITU model and our site-specific model. The use of measured data together with our measurement-based calibration methodology ensured the reliability of the resulting simulation datasets. The extended simulation output provided supplemental data points that were at distances and locations we were unable to measure. According

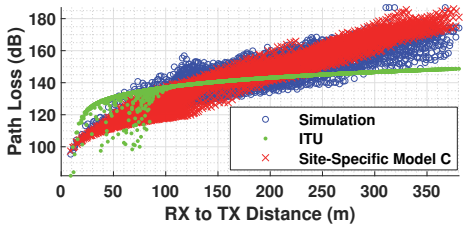

(a) Path loss over RX-to-TX distance

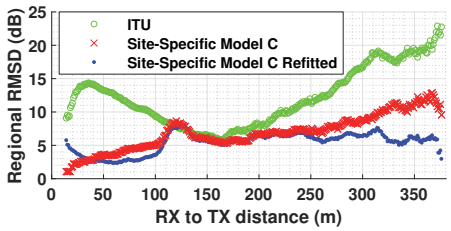

(b) Regional RMSD with respect to the simulation results

Fig. 8. In-forest performance comparisons for the ITU and site-specific models over the extended grid. (a) Both models have a good agreement with simulation results. (b) The regional RMSD was evaluated with a window size of 10 m. The site-specific model clearly works better than the ITU model.

to the simulation, our site-specific model is applicable beyond the region covered by the measurement data and thus provides a very promising approach for mm-wave channel modeling.

The simulation-aided aspect of our work suggests that moderate-fidelity simulation can be used to develop reliable low-complexity mm-wave channel models. We have demonstrated one application of simulation in evaluating and enhancing measurement-based models for mm-wave propagation. With the extremely high sensitivity of mm-wave to environmental features, traditional channel models ignoring site- and link-specific geometry are insufficient. Improved models that are able to automatically identify environment features in geographic datasets and learn key channel parameter values from measurements are the future of mm-wave channel modeling. Given the extremely high cost in both money and time for mm-wave channel measurements, the tremendous amount of channel information that could be provided by simulation is critical in applying state-of-art machine learning techniques into this area. Using a calibrated simulation, we can comprehensively characterize an environment geospatially. In particular, we can generate reliable simulation results for links that we are unable to measure—such as those with path losses in excess of the measurement system's dynamic range or for locations physically impossible to access. In our work, using even a limited measurement dataset to calibrate the simulation engine ensures that the resulting output is valid for use in channel modeling. These measurement-based simulation data can be generated as needed, and utilized, for example, in training a deep learning neural network to save all or a majority of the measurement results as the ground truth testing set. This way of extending usable datasets via measurement-based simulation dramatically relieves the dilemma between data accuracy and cost efficiency.

Another advantage of simulation-aided channel modeling is that simulations can be carried out in advance of or during a measurement campaign to establish areas of interest to focus on and facilitate campaign planning. Locations, environments, and interesting phenomena, such as urban canyons, constructive multipath, or deep fading, can be predicted by simulation beforehand. Those can then be characterized as part of a measurement campaign. By more thoroughly using simulation, we can be sure to have a more comprehensive characterization of an environment with the resultant measurements.

V. Conclusion

In this paper, we examined a simulation engine for mm-wave propagation through foliage with measurement data collected in a coniferous forest. After confirming the engine's validity, simulation results for an extended RX location grid were generated and used for testing the ITU-R obstruction by woodland model and a site-specific model we introduced in our previous work. By shifting from the traditional measurement-only channel modeling approach to including simulation as an aid for obtaining data, we were able to resolve the limits from the measurement system and the environment to show the broader applicability of the site-specific model.

References

[1] S. Rangan, T. S. Rappaport, and E. Erkip, "Millimeter-wave cellular wireless networks: Potentials and challenges," *Proc. IEEE*, vol. 102, no. 3, pp. 366–385, Mar. 2014.

[2] A. F. Molisch *et al.*, "Millimeter-wave channels in urban environments," in *2016 10th Eur. Conf. Antennas Propag. (EuCAP)*, Apr. 2016, pp. 1–5.

[3] X. Wu *et al.*, "60-GHz millimeter-wave channel measurements and modeling for indoor office environments," *IEEE Trans. Antennas Propag.*, vol. 65, no. 4, pp. 1912–1924, Apr. 2017.

[4] C. Umit Bas *et al.*, "Outdoor to indoor propagation channel measurements at 28 GHz," *IEEE Trans. Wireless Commun.*, vol. 18, no. 3, pp. 1477–1489, Mar. 2019.

[5] Y. Zhang *et al.*, "28-GHz channel measurements and modeling for suburban environments," in *2018 IEEE Intl. Conf. Commun.*, May 2018, pp. 1–6.

[6] C. Umit Bas *et al.*, "28 GHz foliage propagation channel measurements," in *2018 IEEE Global Commun. Conf.*, Dec. 2018, pp. 1–6.

[7] Defense Advanced Research Projects Agency. Spectrum collaboration challenge (SC2). Accessed: Apr. 12, 2020. [Online]. Available: https://www.spectrumcollaborationchallenge.com/

[8] N. Gonzalez-Prelcic, A. Ali, V. Va, and R. W. Heath, "Millimeter-wave communication with out-of-band information," *IEEE Commun. Mag.*, vol. 55, no. 12, pp. 140–146, Dec. 2017.

[9] A. Klautau, P. Batista, N. Gonzlez-Prelcic, Y. Wang, and R. W. Heath, "5G MIMO data for machine learning: Application to beam-selection using deep learning," in *2018 Inf. Theory Appl. Workshop (ITA)*, Feb. 2018, pp. 1–9.

[10] A. Alkhateeb, S. Alex, P. Varkey, Y. Li, Q. Qu, and D. Tujkovic, "Deep learning coordinated beamforming for highly-mobile millimeter wave systems," *IEEE Access*, vol. 6, pp. 37 328–37 348, 2018.

[11] Y. Zhang *et al.*, "Improving millimeter-wave channel models for suburban environments with site-specific geometric features," in *2018 Int. Appl. Comp. Electromagn. Soc. Symp. (ACES)*, Mar. 2018, pp. 1–2.

[12] Y. Zhang, C. R. Anderson, N. Michelusi, D. J. Love, K. R. Baker, and J. V. Krogmeier, "Propagation modeling through foliage in a coniferous forest at 28 GHz," *IEEE Wireless Commun. Lett.*, 2019.

[13] J. Tan, Z. Cao, L. Carlson, L. Barbieri, and J. Lunn, "Modeling and analysis of RF propagation in complex environments," in *Proc. IEEE MILCOM*, Orlando, Oct. 2015.

[14] International Telecommunication Union, *Recommendation ITU-R P.833-9 Attenuation in Vegetation*, Std., Sep. 2016, Accessed: Apr. 12, 2020. [Online]. Available: https://www.itu.int/rec/R-REC-P.833-9-201609-I/en

[15] SciX^3, LLC, "Foliage propagation model development to support new communications concepts: Phase II final report," Defense Advanced Research Projects Agency, VA, USA, Tech. Rep., contract no. W31P4Q-14-C-0014, Sep. 2018, to be published.